

# Urban dynamics through the lens of human mobility

---

In the format provided by the  
authors and unedited

**This PDF file includes:**

Supplementary Sections 1 to 6

Supplementary Figures 1 to 19

Supplementary Tables 1 and 2

References

# Supplementary Sections

## 1 List of variables and notations

$Rg$  Radius of gyration, defined as  $Rg = \sqrt{\sum_{i=1}^n \frac{1}{n}(\mathbf{l}_i - \mathbf{l}_h)^2}$ , where  $n$  is the total number of visited locations for an individual during a given day,  $\mathbf{l}_i$  are the coordinates in position  $i$ ,  $\mathbf{l}_h$  are the coordinates of her home,  $\mathbf{l}_i - \mathbf{l}_h$  denotes the distance of the location  $\mathbf{l}_i$  away from home, as illustrated in Fig. 2A in the main text. Note that the repeatedly visited locations are kept in the calculation of  $Rg$ . To present the distribution of  $Rg$  in space before the COVID-19 pandemic, as shown in Figs. 1B-D, Supplementary Figs. 3 and 5, we first exclude the days on which  $Rg = 0$  and then average individual's daily  $Rg$  over the various data availability periods ranging from one month to 6 months. The unit of  $Rg$  is kilometers.

$r$  Radius of the ring centering at CBD. The internal radius of the concentric rings from the CBD with width  $\Delta r = 3$  km. That is, the first ring covers the circular region in 3 km distance to the CBD; the second one covers the circular region between 3 km and 6 km from the CBD, as illustrated in Fig. 2C. The unit of  $r$  is kilometers.

$KS(\hat{r}|r_0)$  Kolmogorov–Smirnov (KS) distance between  $Rg$  values of the population residing in the ring at the relative distance  $\hat{r}$  to the CBD and  $Rg$  values of the population in the circle of CBD, as illustrated in Fig. 2C and 2D in the main text.  $KS(\cdot)$  denotes the KS distance that quantifies the statistical divergence between two groups of data with their cumulative distributions. For a given city, the relative distance  $\hat{r}$  is defined as the ratio between the radius of the

ring  $r$  and the maximum radius  $r_{max}$  of the city,  $\hat{r} = r/r_{max}$ . Fig. 3C in the main text shows the  $KS(\hat{r}|r_0)$  during typical period with no occurrence of large-scale emergencies for each city.

$\Delta KS$  Mobility centrality index, defined as the gradient of KS statistic between  $Rg$  in rings and  $Rg$  in the CBD circle,  $\Delta KS(\hat{r}) = \frac{\partial KS(\hat{r})}{\partial \hat{r}}$ .  $\Delta KS$  is simply calculated as the slope of linear fitting between  $KS(\hat{r})$  and  $\hat{r}$ , as shown in Fig. 2E in the main text.  $\Delta KS$  is introduced to quantify the influence of city centers on the mobility scale of the population.

$KS_{HBT}$  Measurement of the extent of home-based-travel for the residents, defined as the Kolmogorov–Smirnov statistic between the distribution of the observed  $Rg$  of the population and the distribution of  $Rg$  if all population would be staying at home, as illustrated in Fig. 2F. We assume  $Rg$  as a random value between 0 and a given threshold  $r_{shelter}$ , if an individual is staying at home. A lower  $KS_{HBT}$  indicates more people are staying at or near home.

$r_{shelter}$  Mobility radius of people following the travel restriction order. For the selection of the distance threshold  $r_{shelter}$ , we show the change of median  $Rg$  during the eight months from the outbreak of COVID-19 pandemic in the Spanish cities in Supplementary Fig. 16. We can see that, during the lockdown, the median  $Rg$  of the population is near 0.5 km on weekdays in all cities. We also show the median  $Rg$  and the 25%-75% confidence interval for typical large cities (Madrid and Barcelona) and small cities (Malaga and Alicante). The median  $Rg$  in these typical cities is clearly around 0.5 km during lockdown. In addition, the spatial resolution of pinpointing users with the locations of antennas in CDR data could be 300 meters in rural areas. Therefore, we need

to select a distance threshold over 300 meters. From these perspectives, as we can consider that more than half the population was following the shelter-at-home order during the lockdown, the median value of  $Rg$  (0.5 km) can be a reasonable threshold to identify the extent of home-based-travel.

$\overline{Rg}_{typ}$  Typical  $Rg$ , defined as the average  $Rg$  during typical period with no occurrence of large-scale emergencies. For the studied Spanish cities, the typical period means the time before the outbreak of the COVID-19 pandemic, when there are no travel restrictions executed. Specifically, we calculate  $\overline{Rg}_{typ}$  by averaging the daily  $Rgs$  of population during October 2019 in Spain. For other cities,  $\overline{Rg}_{typ}$  is calculated on the data periods we have. The unit of  $\overline{Rg}_{typ}$  is in kilometers.

$\Delta KS_{typ}$  Typical mobility centrality index  $\Delta KS$ , calculated during a typical period with no occurrence of large-scale emergencies, same as  $\overline{Rg}_{typ}$ .

$\overline{Rg}^{7d}$ . Average value of the daily  $Rg$  in the seven days before the  $d$ th day,  $\overline{Rg}_{7d} = \sum_{d-6}^d Rg^d / 7$ , as illustrated in Supplementary Fig. 18.

$\Delta KS^{7d}$  Average value of the daily  $\Delta KS$  in the seven days before the  $d$ th day.  $\Delta KS^{7d} = \sum_{d-6}^d \Delta KS^d / 7$ , as illustrated in Supplementary Fig. 18.

$KS_{HBT}^{7d}$  Average value of the daily  $KS_{HBT}$  in the seven days before the  $d$  day.  $KS_{HBT}^{7d} = \sum_{d-6}^d \Delta KS_{HBT}^d / 7$ , where  $\Delta KS^d$  refers to the observed  $\Delta KS$  on the  $d$  day, as illustrated in Supplementary Fig. 18.

$R_t$  Daily effective reproduction number of COVID-19, calculated on the daily reported cases in a sliding 7-day window, as illustrated in Supplementary Fig. 15. The estimation is implemented with the *EpiEstim* R package for each

selected province in Spain (*I*) and the results are presented in Supplementary Fig. 19.

## 2 Urban mobility retrieved from CDRs

For the studied cities with CDRs data, the users' visited locations are not completely recorded when they are not using cell phones. Therefore, we use an urban mobility model, TimeGeo, to retrieve the daily travel behavior of users in Boston, San Francisco Bay Area, Los Angeles, Bogotá, Lisbon, and Porto. TimeGeo is a fine-scale mobility model that replies on the long-term records of trajectory data to infer the user's visited locations every 10 minutes in a typical week (2).

To this end, we first detect the stay locations by clustering the footprints in one user's consecutive trajectory. The threshold in spatial clustering is set as 500m. The centroid of a cluster of points is regarded as a stay location if the timespan in the cluster exceeds 10 minutes, suggesting that the user has stayed in this location at least for 10 minutes. Other footprints are labeled as pass-by and neglected in our further analysis. Second, among all stay locations for each user, we identify the home location by finding the most frequently visited place on weekends and during the nights of weekdays. Users are removed if there is no dominant place during these periods, meaning that they are probably visitors to the city as there is no home location found. Similarly, we identify the user's work location by finding the dominantly visited place during the daytime (10:00 - 17:00) on weekdays. Consequently, all stay locations of users are labeled as *home*, *work*, or *other*. Users are labeled as commuters if their workplaces are available, and others are labeled as non-commuters.

The TimeGeo modeling framework adopts three parameters to define the temporal choices of travel activity through a time-inhomogeneous Markov chain model for each user. The parameters are individual-specific, including weekly home-based tour number ( $n_w$ ), dwell rate ( $\beta_1$ ),

and burst rate ( $\beta_2$ ). Also, the global travel circadian rhythm of the population in an average week,  $P(t)$ , is introduced to guarantee that the modeling of individual users' travel behavior can follow the collective mobility behavior at the urban scale. For the spatial choices of users' destinations, TimeGeo uses a rank-based exploration and preferential return (r-EPR) model to choose destinations for every non-commuting trip by ranking their visited frequencies and distances to the origins. More details about the TimeGeo model can be found in (2). After running TimeGeo model on each active mobile phone user, we expand these users to the entire population with the two expansion factors in each census tract. For each census tract, we define commuter (non-commuter) expansion factor as the ratio between the actual number of commuters (non-commuters) from census data and the number of active phone users, who are labeled as commuters (non-commuters) and settling in the same census tract. As TimeGeo is a probability model, even though users share the same set of parameters after expansion, they perform different travel behavior in the simulation. TimeGeo model has been validated in Boston, SF Bay Area, Los Angeles, and Bogotá, using the travel survey data and can successfully reconstruct the mobility behavior at both individual and collective levels compared with the travel surveys (2–4).

### 3 Dynamic racial and economic segregation

Since isolation entails which neighborhoods individuals visit, we leverage our mobility data to assess the extent of social segregation within the city. To do so, we first use the information theory index  $H$  (5, 6), to create a segregation profile over 24 hours. Defining the proportion of population  $\pi_{jr}$  of each race  $r \in R$  within a spatial unit  $j$ , then the entropy  $E_j$  is written as follows:

$$E_j = - \sum_{r \in R} \pi_{jr} \ln \pi_{jr} , \quad (1)$$

and the  $H$  index is defined as:

$$H = \frac{E - \sum_{j \in J} \frac{p_j}{P} E_j}{E} , \quad (2)$$

where  $E$  is the entropy of the racial composition of the entire city,  $E_j$  is the entropy of the racial composition in spatial unit  $j$ ,  $J$  is the set of all spatial units considered within the area,  $P$  is the total population, and finally,  $p_j$  is the population in the spatial unit  $j$ . Interpreting entropy as a measure of diversity, the segregation index  $H$  is the population-weighted difference between the diversity of each spatial unit and the diversity of the whole city.  $H$  index varies from 1 to 0. It is equal to 1 if there is maximum segregation, meaning that every spatial unit is populated by only one race. On the contrary, if each race is distributed uniformly throughout the total region, there is no segregation and the  $H$  index equals 0. After reviewing  $E$  and  $H$  for the two United States cities, we find that Los Angeles is both more diverse and more segregated than Boston.

We then measure the  $H$  index throughout the day. The resulting temporal evolution is shown in Supplementary Fig. 4A. In line with some previous studies (7–9), we find that spatial segregation is significantly higher during the night (from 20:00 to 5:00) than during the day (between 9:00 and 16:00). When comparing maximum and minimum values, the  $H$  index is found to decrease by 50% in Boston and LA, and 70% in Bogotá. The mixing occurs in the employment subcenters but we cannot see any difference among mono/polycentric cities.

Despite mobility dynamics tend to promote mixing between demographic groups, considerable spatial separation remains. That is, all cities are imperfectly mixed ( $H \neq 0$ ). Two main factors can explain this result. The first factor is the strong residential segregation patterns, which coupled with limited travel radii avoids the perfect mixing. The second is the hypothetical existence of homophily in daily mobility; individuals could tend to visit neighborhoods with similar race composition to their home neighborhood during their leisure time. We then further explore these factors by calculating the racial composition of visitors of each tract. This measure allows us to quantify how the attractiveness of a given location depends on its racial

composition. In Supplementary Fig. 4B, we show the difference between the non-commuting visitors and global proportion of each socio-economic group in Bogotá. In Supplementary Figs. 4C and 4D, for each racial group, we plot the average share of non-commuting visitors with race  $r_j$  for a location depending on the share of the population of its primary race  $r_i$  in Boston and LA, respectively. In this analysis, we have focused only on trips related to non-work activities (leisure time).

Since the surrounding areas of a neighborhood with a majority race  $r_i$  are less diverse than the entire city, we can expect a higher representation of the race  $r_i$  among its visitors. Overall, we observe that for all races in both Boston and LA, see Supplementary Figs. 4C and 4D. Thus, we can interpret the first point in those curves as an effect of the residential segregation patterns. However, in some cases, the higher the share of residents with race  $r$  is, the higher the share of visitors of the same race. We interpret this behavior as homophily. Interestingly, Hispanics show homophily in both cities, regardless of whether, in one case, they are the majority group (LA) and, in the other, a minority group (Boston). Whites, in turn, show homophily in Boston, but in Los Angeles seem to be indifferent to the actual share of whites in the recipient tract. Finally, Blacks show an imperceptible homophily behavior in both cities. Regarding pairwise relationships of different racial groups to each other, it is worth noting that, in Boston, the representation of Hispanic visitors in Black neighborhoods is higher than the global Hispanic share. In other words, in that city, Hispanics have a certain affinity for neighborhoods with Black majority. Being a minority in both cities, Black residents show an imperceptible homophily.

## 4 Comparison of varying measures for mobility centrality

### 4.1 Cumulative measure of people's mobility behavior

In Fig. 2C, we group the population in one city with a series of concentric rings. There is no overlapping population among these rings. Such concentric rings are meant to capture the in-

fluence of the distance from the CBD on people’s mobility behavior. Here, we also attempt a cumulative measure to represent the statistical change in people’s mobility behavior in a city. Specifically, we define a series of circles centering at CBD with increasing radii, as shown in Supplementary Fig. 10A. Then we compare the statistical divergence between people residing in these circles. The outer circles cover the population in the inner circles. The Kolmogorov–Smirnov ( $KS$ ) distance between the  $Rg$  values of the population residing in the outer circles and the CBD circle is presented in Supplementary Fig. 10B. As expected, the change of  $KS$  is much more smooth than our original measure based on rings. The relation between  $KS$  distance and the radii is more like a power-law function than a linear function. Therefore, we fitted the curves in 21 cities with a power-law function,  $Y \sim \alpha \cdot X^\beta$ . From Supplementary Fig. 10B, we can observe a sublinear relation for most cities ( $\beta < 1$ ). We thus regard the exponent  $\beta$ , as the mobility centrality indicator to describe the urban spatial structure. The results are given in Supplementary Fig. 10C. From this figure, we observe that the urban spatial structure of Boston (a typical monocentric city) falls between two polycentric cities (Los Angeles and Barcelona), suggesting the infeasibility of this cumulative measure.

Another weakness of cumulative measure is that, the population distribution heavily impacts the  $KS$  distance between two circles, because the outer circle covers the population in the inner circle. In our work, we desire to decouple the distribution of population and urban dynamics into a two-dimensional space. Even if fewer inhabitants are residing in the area away from the CBD, we still want to measure their mobility behavior. Therefore, the rings without population overlapping are a better measure.

## 4.2 Measuring urban structure with varying statistical metrics and different fitting functions

In Fig. 2D, we measure the statistical divergence of the  $Rg$  values of two groups of population with the Kolmogorov–Smirnov ( $KS$ ) distance. Here, we empirically compare  $KS$  distance with three other statistical distances. Namely: (i) the relative change of  $Rg$  ( $Rg_{relative}$ ); (ii) the Jensen–Shannon divergence ( $JSD$ ), and (iii) the Kullback–Leibler divergence ( $KL$ ). Each statistical distance was used to measure the divergence between  $Rg$  values of the population in the CBD circle and outer rings. Note that  $KS$  distance is calculated based on CDFs of two sets of data, such that it can measure the statistical distance between two sets with different lengths. In contrast, the other two commonly used metrics,  $JSD$ , and  $KL$  distances require the same length for two inputs. Therefore, when we apply  $JSD$  and  $KL$  distances, we first calculate the discrete probability distributions (histograms) of the two datasets for comparison to scale them to the same length. Then we compare the divergence between the two histograms with  $JSD$  or  $KL$ . Besides,  $KL$  distance is also an asymmetric metric, which means that  $KL(A, B) \neq KL(B, A)$ , in most cases. Such an asymmetric metric is inappropriate to measure divergence between two groups of the population.

In addition, for a more comprehensive comparison, we fit the relation between  $KS$  and the distances to CBD with both linear and power-law functions, as illustrated in Fig. 3C. Regarding the power-law function  $Y \sim \alpha \cdot X^\beta$ , we use the fitted exponent  $\beta$  as urban mobility centrality, to describe the urban spatial structure. We can imagine that a larger  $\beta$  indicates a more monocentric urban structure, as people’s trip lengths increase more strongly with their distance to CBD. While for the linear function, we use the slope of the fitting as the urban structure indicator. In summary, we comprehensively compared eight combinations of “statistical distance + fitting function” to describe urban spatial structure. The corresponding urban dynamic metric and the r-square of the fitting are presented in Supplementary Figs. 11A and 11B.

From Supplementary Fig. 11A, we observe that the indicators of most combinations can be over 1, except for “*JSD* + Linear” and “*KS* + Linear”. We prefer our centrality indicator to be a value from 0 to 1. From this perspective, only “*JSD* + Linear” and “*KS* + Linear” are kept for future consideration. Secondly, we expect all cities to have acceptable goodness-of-fit in the linear fitting. Results are shown in Supplementary Fig. 11B. For “*JSD* + Linear”, we can see that San Francisco Bay Area is an outlier, with a very low  $r^2 = 0.1713$ . While for “*KS* + Linear”, despite a relatively lower  $r^2$  for San Francisco Bay Area in comparison with other cities, its value reaches 0.4774 and is still much better than “*JSD* + Linear”. In summary, the “*KS* + Linear” is a better indicator to describe people’s mobility centrality with respect to the CBD.

In Supplementary Fig. 11C, we also present the comparison between the power-law exponent and the slope of linear fitting for the *KS* statistics. We see that the exponent of the power-law fit and the slope of linear fit generally have a positive correlation, with a clear exception for Barcelona. Intuitively, a larger exponent means the change of  $R_g$  is faster as a function of the distance to the CBD, indicating a monocentric urban structure. But for Barcelona, a typical polycentric city, the exponent is the largest among the 21 cities. Another exception is Zaragoza, whose population is compact in the CBD. But its exponent of power-law fitting is very close to Shenzhen, a polycentric city. In contrast,  $\Delta KS$  based on linear fitting behaves as we expect. That is, the slope of the linear fit is a more feasible indicator of urban spatial structure in comparison with the power-law exponent. For the power law fitting, we would need a more sophisticated design to reach a reasonable metric.

## 5 Estimate of time-varying $R_t$ from daily reported cases

In this work, we use the *EpiEstim* R package to estimate the effective reproduction number of COVID-19 pandemic in the selected Spanish cities (10). *EpiEstim* is an open-source R package

to estimate the time-varying reproduction number  $R_t$  of an epidemic from the incidence time series and has been adopted to estimate the transmission intensity of Ebola virus, Zika virus, and SARS-CoV-2 in various countries (11–15).

In *EpiEstim*, the time-varying reproduction number  $R_t$  and its statistic uncertainty is estimated based on the number of suspected COVID-19 cases every day. *EpiEstim* first defines a probability distribution  $\omega_s$  to represent the probability of individuals showing an infectivity profile once he or she is infected.  $\omega_s$  is then approximated by the distribution of a *serial interval*, which is defined as the time difference between the onset of the symptoms of a primary case and her corresponding secondary cases. Therefore,  $\omega_s$  depends on the duration time since the infection of the case,  $s$  days, but is independent of the time she gets infected. Here, we follow the observation from (16), assuming the *serial interval* distribution as a discrete Gamma distribution, with a mean of 3.6 days and a standard deviation of 4.9 days. Then, the expectation of the newly infected population is updated by,

$$\mathbf{E}[I_t] = R_t \sum_{s=1}^t I_{t-s} \omega_s \quad (3)$$

where  $I_t$  and  $I_{t-s}$  denote the number of newly infected population on the time step  $t$  and  $t - s$ , respectively;  $\mathbf{E}[X]$  denotes the expectation of a sequence of random variables  $X$ . Then we can estimate  $R_t$  with

$$R_t = \frac{I_t}{\sum_{s=1}^t I_{t-s} \omega_s} \quad (4)$$

By assuming the prior distribution of  $R_t$  is a Gamma-distribution, the Bayesian inference based on this transmission model leads to a simple analytical expression of the posterior distribution of  $R_t$ .

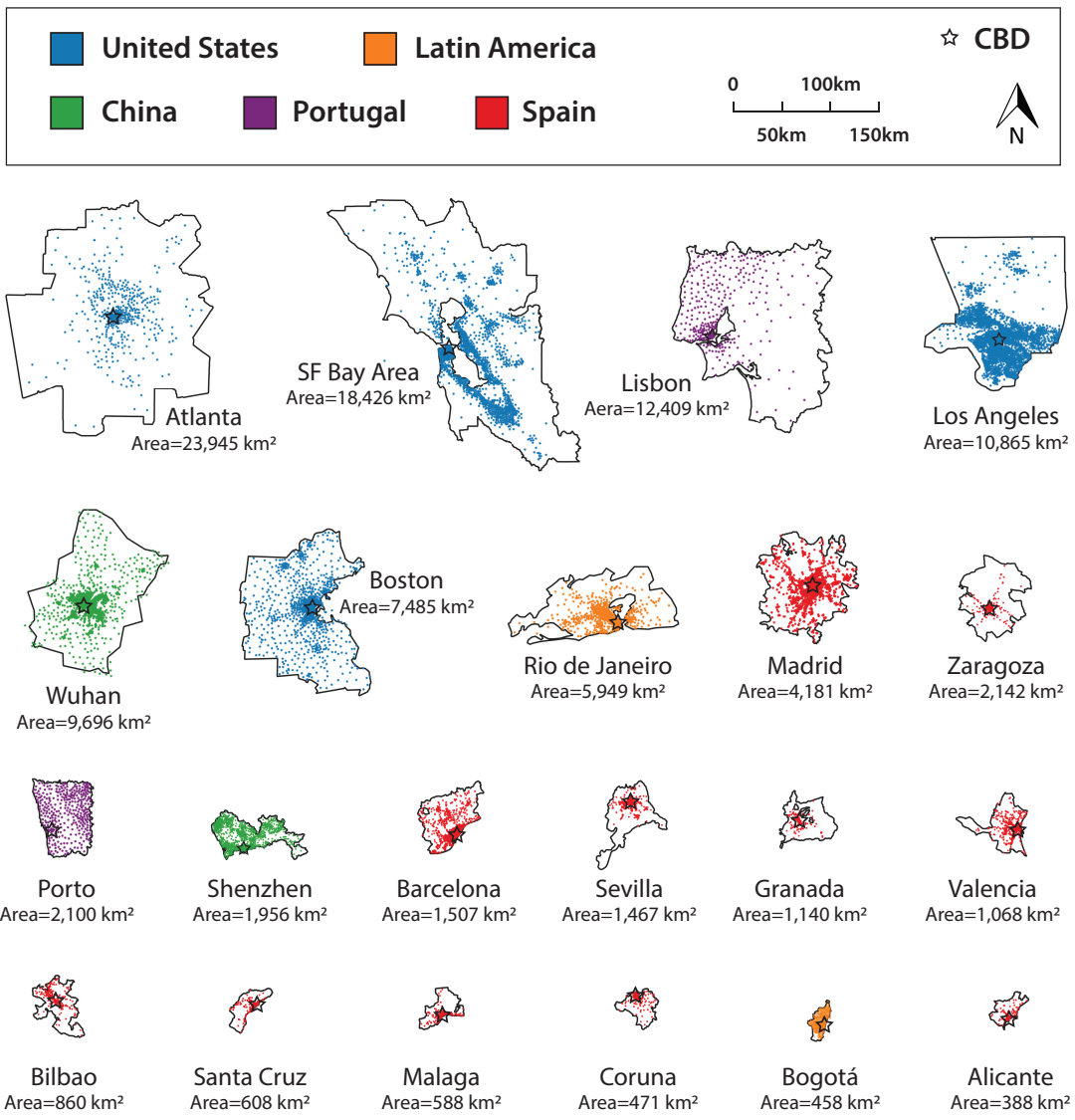
As the newly reported number of cases deviates from the actual number due to the delayed and limit accuracy of testing, the estimate  $R_t$  can be highly variable. Given this, *EpiEstim* provides a way to measure  $R_t$  over a time period,  $R_{t,\tau}$ , where  $\tau$  is the size of the window in

which the  $R_t$  is calculated. One can expect that  $R_{t,\tau}$  would be less variable and more precise as the window size  $\tau$  increases. Following the parameters used by Abbott et al. (13), we used a Gamma distribution with mean of 2.6 and a standard deviation of 2.0, as the prior distribution of  $R_t$ . The time slot in our case of COVID-19 is one day, indicating we fit the model with the daily reported number of cases. We used a seven-day time window ( $\tau = 7$  days) before the day  $t$  to calculate the reproduction number for each province in Spain, written as  $R_t$ . More details about the implementation of *EpiEstim* can be found in (10).

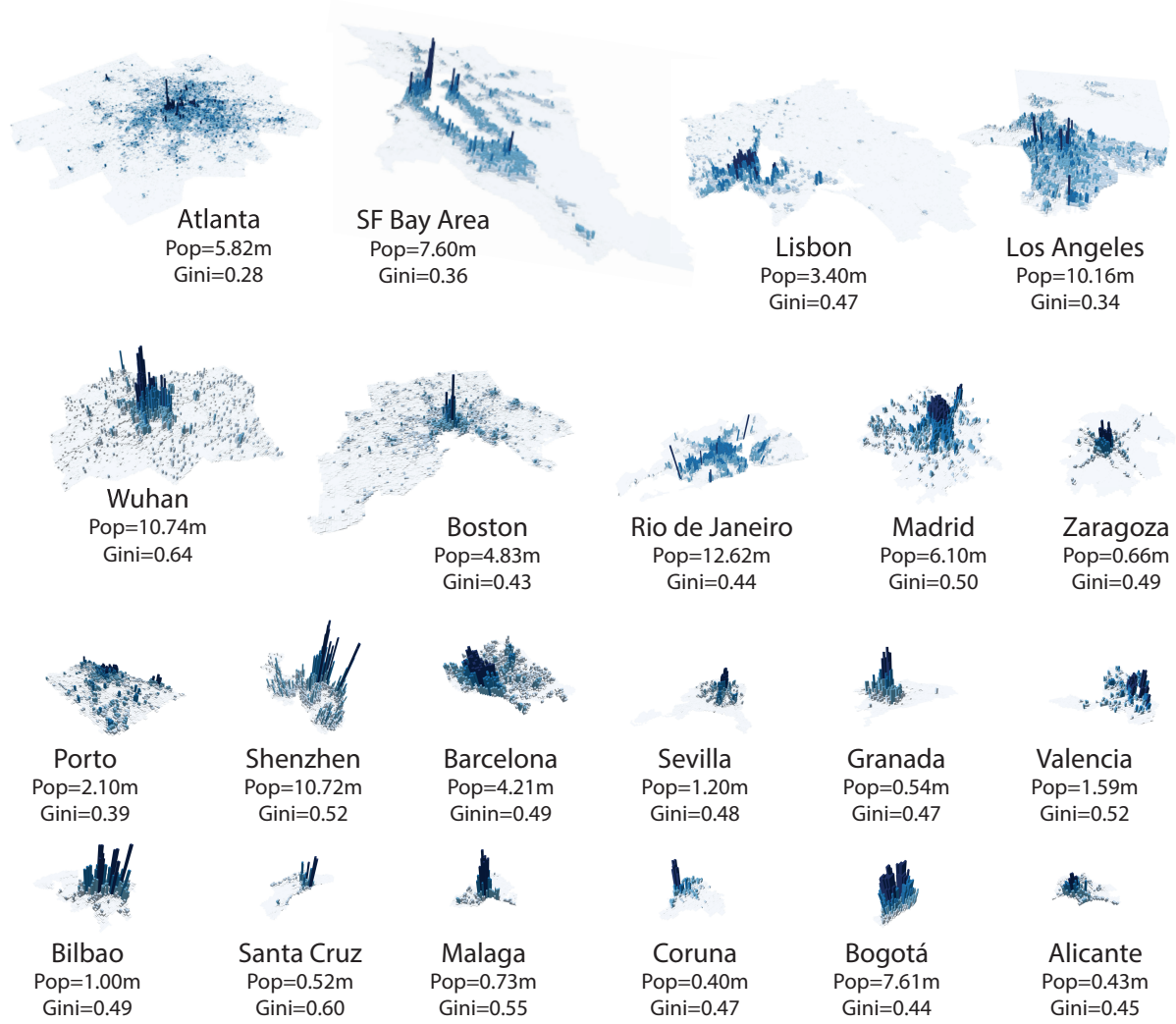
We obtained the daily reported cases of COVID-19 in Spain at the province level, collected by *montera34.com*, original from the ministry of health of each province<sup>1</sup>. Note that as the daily reported cases at the city level are not publicly available, we assume that the city has the same  $R_t$  as its province. The proportion of the population of the province that resides in the city is shown in Supplementary Table 2. In Supplementary Fig. 15, we illustrate the daily reported cases of COVID-19 and the 7-day average values in the 11 provinces before September 30th, 2020. The estimated  $R_t$  and the 95% confidence interval in each city are illustrated in Supplementary Fig. 19.

---

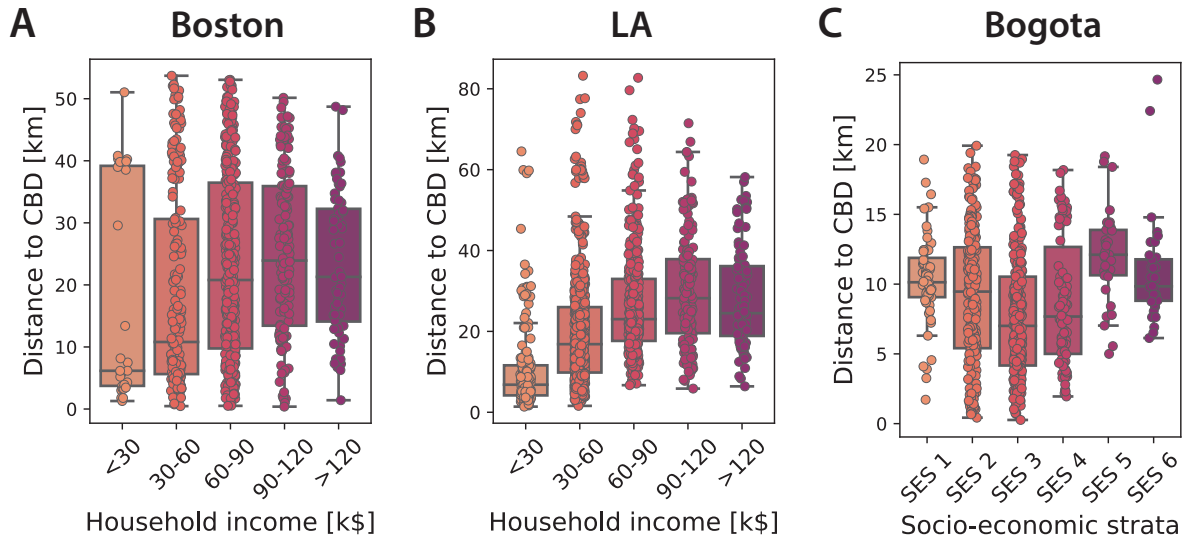
<sup>1</sup><https://github.com/montera34/escovid19data>



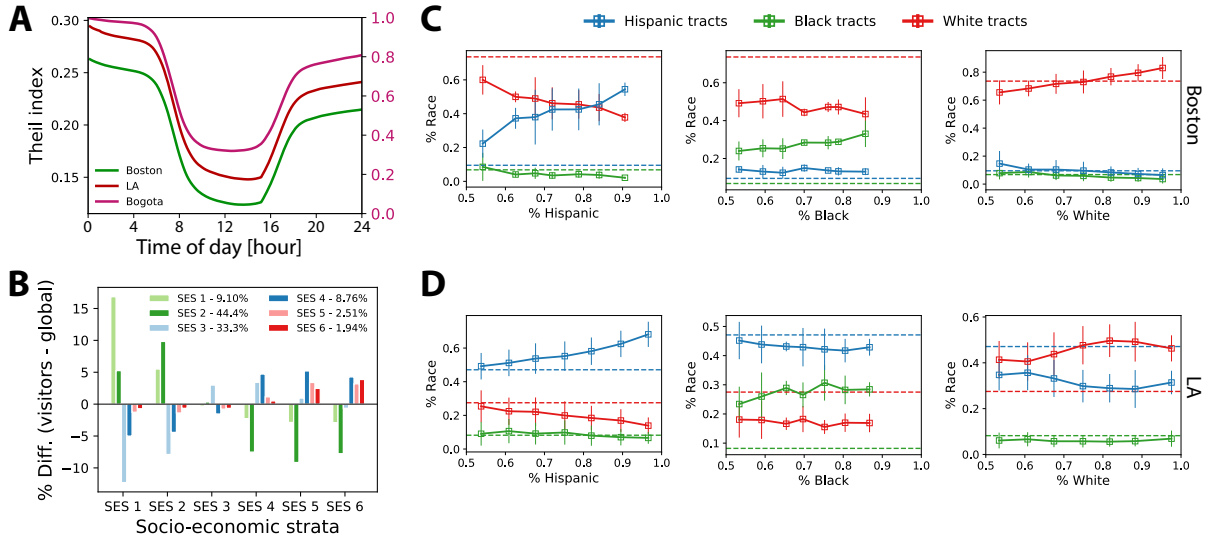
**Supplementary Fig. 1. Urban area footprints of the twenty one cities.** Cities are plotted on the same scale and ordered in terms of area. The points represent the home locations of the anonymized participants in the travel survey in Atlanta and Rio de Janeiro and represent the locations of mobile phone towers in other cities. The points are colored by country.



**Supplementary Fig. 2. Population distributions in the twenty one cities.** Cities are sorted in the same order as Supplementary Fig. 1. The total population and the Gini index of the population are presented for each city.



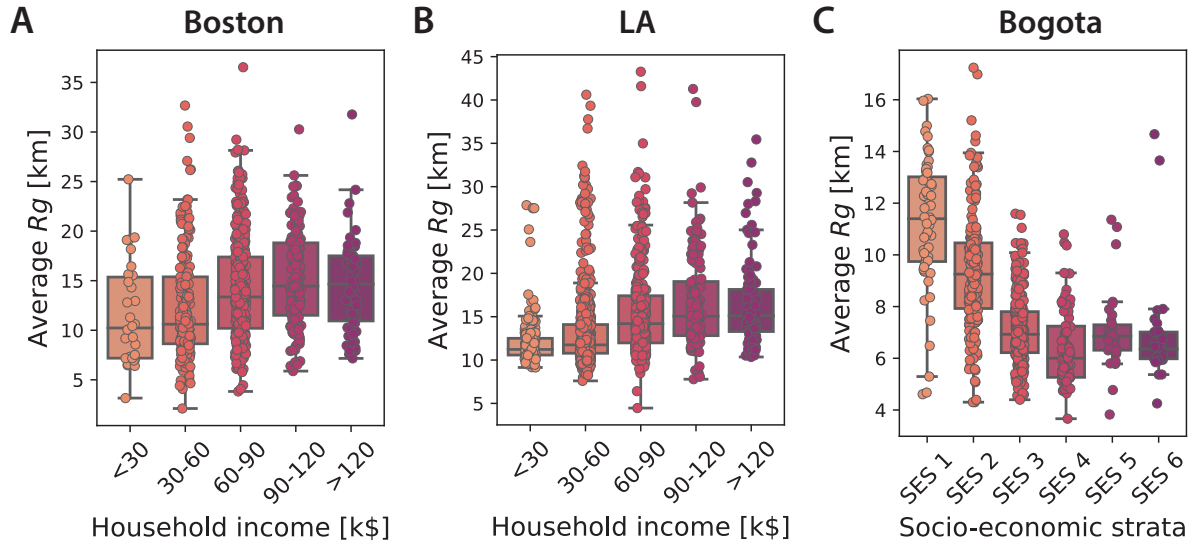
**Supplementary Fig. 3. Box plot of census tracts' distances from CBD for different income groups in Boston, LA, and Bogotá.** Each dot in the box plot represents a census tract, and the tracts are split into different groups by household annual income. In the box plot, centre presents the median value of distance to CBD for each income group; the bounds of box present the 25th and 75th percentile; whiskers present the interquartile range (IQR). In Boston and LA, population with higher income resides further from CBD than a population with lower income. In Bogotá, although there is noticeable income segregation, the relation between income levels and distance to the CBD is not as clear as in the two U.S. cities, as presented in Fig. 1A. In Boston (A), there are 782 tracts with income information, and the number of tracts in each income group is 30, 200, 339, 146, and 67. In LA (B), there are 1,700 tracts with income information, and the number of tracts in each income group is 179, 874, 395, 154, and 98. In Bogotá (C), there are 703 tracts with income information, and the number of tracts in each income group is 56, 213, 282, 82, 34, and 36.



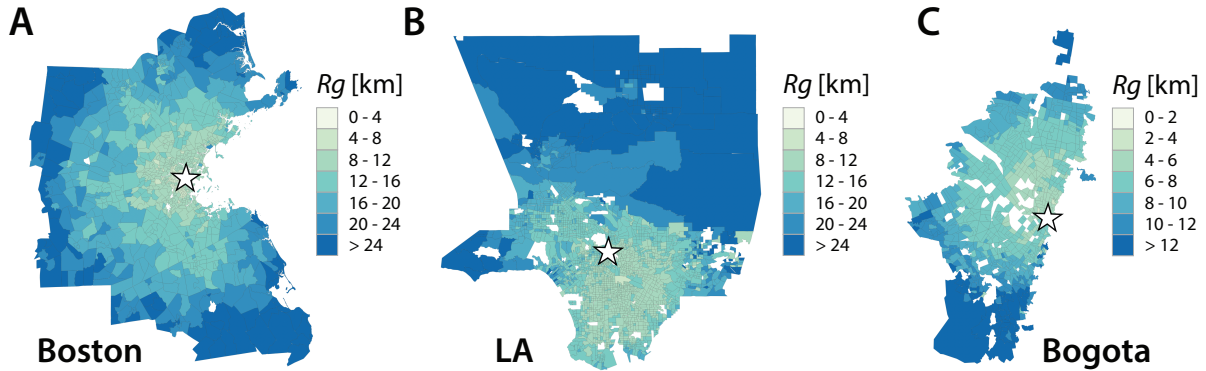
#### Supplementary Fig. 4. Mobility behavior of users in different racial and economic groups.

(A) Evolution of the  $H$  index in three metropolitan regions during the day. (B) Difference between the visitors and global proportion of each socio-economic group in Bogotá. (C) The average share of non-commuting visitors of each racial group in Boston. This measure quantify how, for each race, the attractiveness of given location depends on its own racial composition. We focus on neighborhoods where there is a majority racial group ( $> 50\%$ ). In that way, in each column (departing tract), we are considering disjoint subgroups of tracts. The rectangle marker means the mean fraction of each race in visitors' destination tracts, and the error bar means the standard deviation. In the plot for Hispanic tracts, the number of non-commuting visitors depart from each Hispanic tract from left to right are 3,243, 3,810, 2,015, 4,520, 3,836, 2,612, 1,108. In the plot for Black tracts, the number of non-commuting visitors depart from each Black tract from left to right are 1,138, 2,739, 4,673, 2,553, 1,428, 1,089, 3,220. In the plot for White tracts, the number of non-commuting visitors depart from each White tract from left to right are 1,870, 2,947, 2,879, 3,631, 2,735, 3,846. (D) Average share of non-commuting visitors of each racial group in LA. The rectangle marker means the mean fraction of each race in visitors' destination

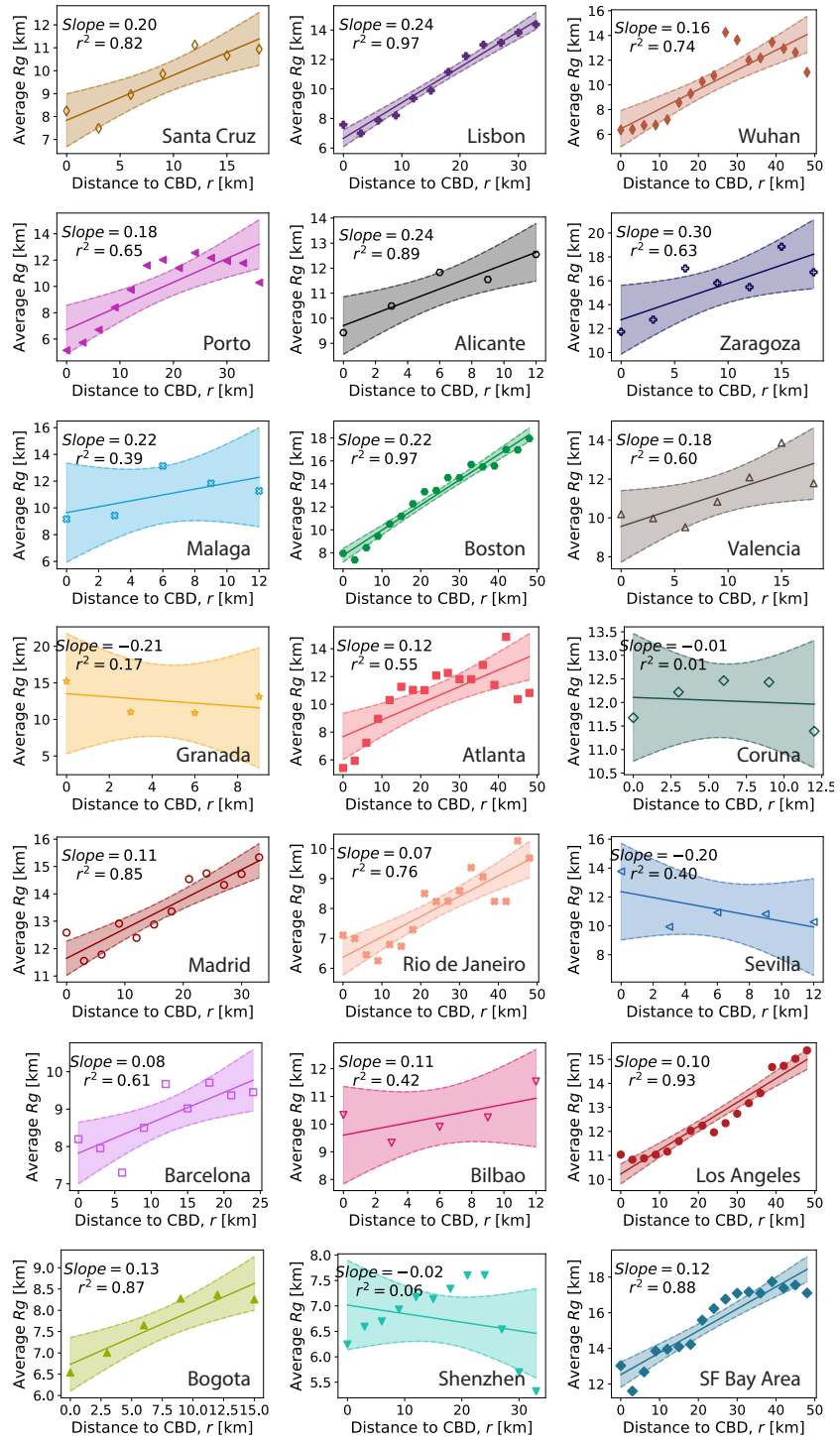
tracts, and the error bar means the standard deviation. In the plot for Hispanic tracts, the number of non-commuting visitors depart from each Hispanic tract from left to right are 2,839, 2,459, 3,741, 2,629, 2,017, 3,297, 2,918. In the plot for Black tracts, the number of non-commuting visitors depart from each Black tract from left to right are 2,774, 2,348, 2,078, 3,258, 1,627, 3,125, 2,241. In the plot for White tracts, the number of non-commuting visitors depart from each White tract from left to right are 2,794, 3,216, 2,129, 3,316, 2,159, 1,956, 1,736.



**Supplementary Fig. 5. Box plot of the average  $R_g$  of census tracts for different income groups in Boston, LA, and Bogotá.** Each dot in the box plot represents a census tract, and the tracts are divided into different groups by their household annual income. In the box plot, centre presents the median value of distance to CBD for each income group; the bounds of box present the 25th and 75th percentile; whiskers present the interquartile range (IQR). In Boston (A), there are 782 tracts with income information, and the number of tracts in each income group is 30, 200, 339, 146, and 67. In LA (B), there are 1,700 tracts with income information, and the number of tracts in each income group is 179, 874, 395, 154, and 98. In Bogotá (C), there are 703 tracts with income information, and the number of tracts in each income group is 56, 213, 282, 82, 34, and 36.

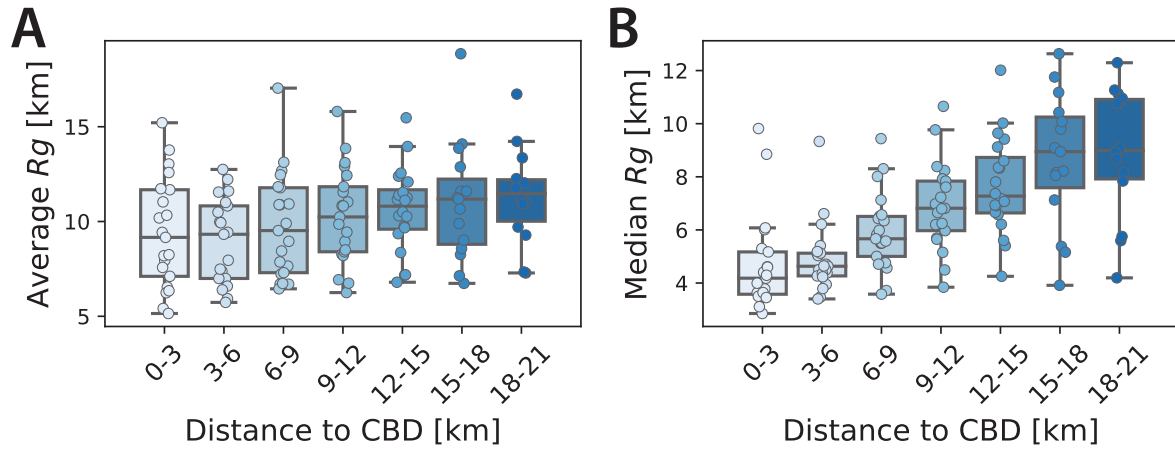


**Supplementary Fig. 6. Average  $R_g$  of per census tract in Boston, LA and Bogotá.** People residing in tracts close to the CBD tend to explore regions near their home locations, while residents in suburban areas travel longer distances. Moreover, the change of average  $R_g$  with respect to the distance to CBD varies among these three cities. As a monocentric city, the average  $R_g$  in Boston increases faster than the other two cities with the distance to CBD.



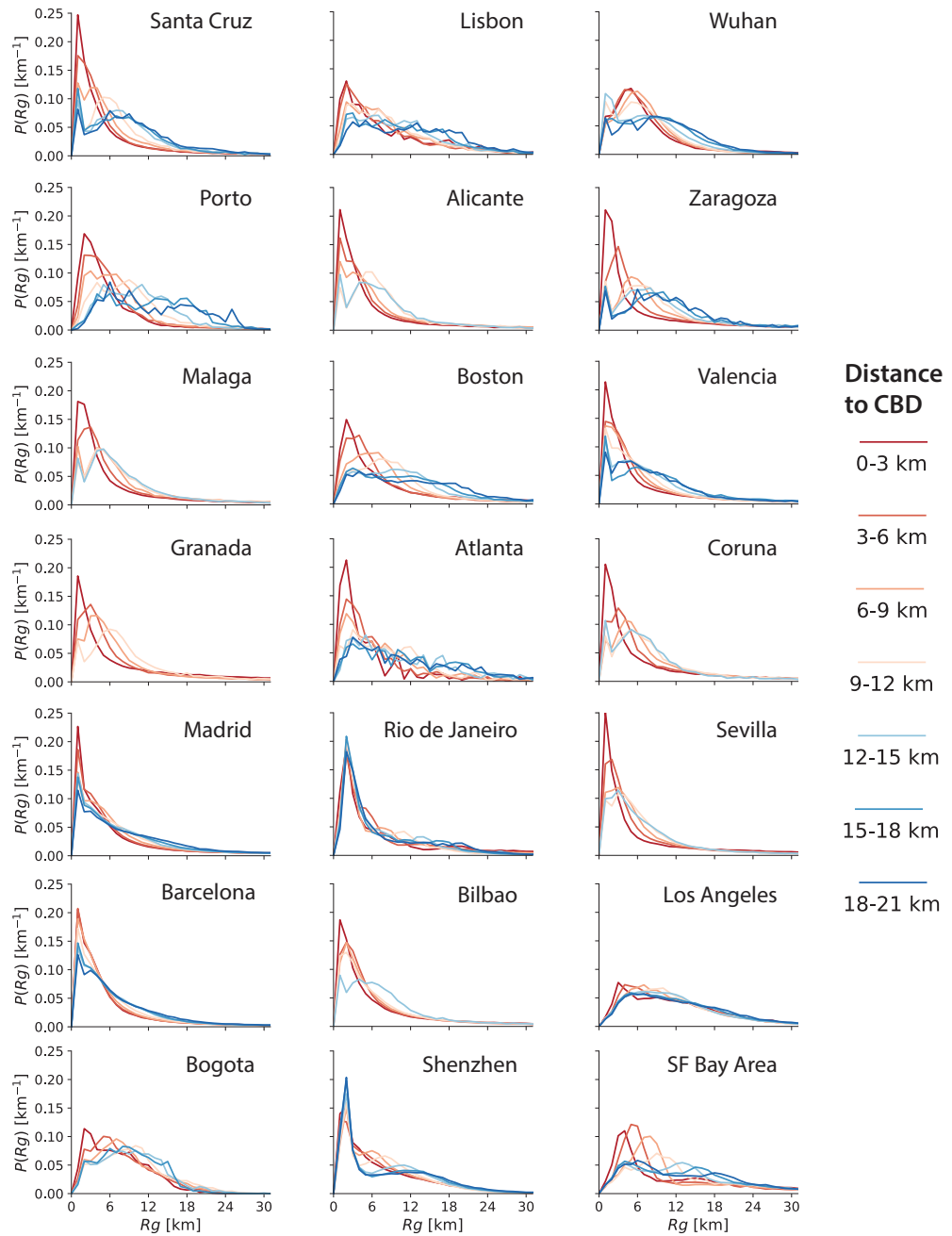
**Supplementary Fig. 7. Relation between the average  $R_g$  and the radii of rings.** Markers in

each panel present the average  $Rg$  in rings with varying radii (distance to CBD). Color bands depict the 95% confidence intervals of the linear fitting. Overall, there is a noticeable increase in  $Rg$  with increasing  $r$ , indicating that individuals living farther from the central business district tend to take longer trips as part of their daily routines. Results indicate that, in certain cities such as Lisbon, Boston, Madrid, and Los Angeles, there is a clear linear relationship between the average  $Rg$  and the radius  $r$ . However, in other cities such as Malaga, Granada, La Coruna, Sevilla, and Bilbao, this linear relationship cannot always be assumed.

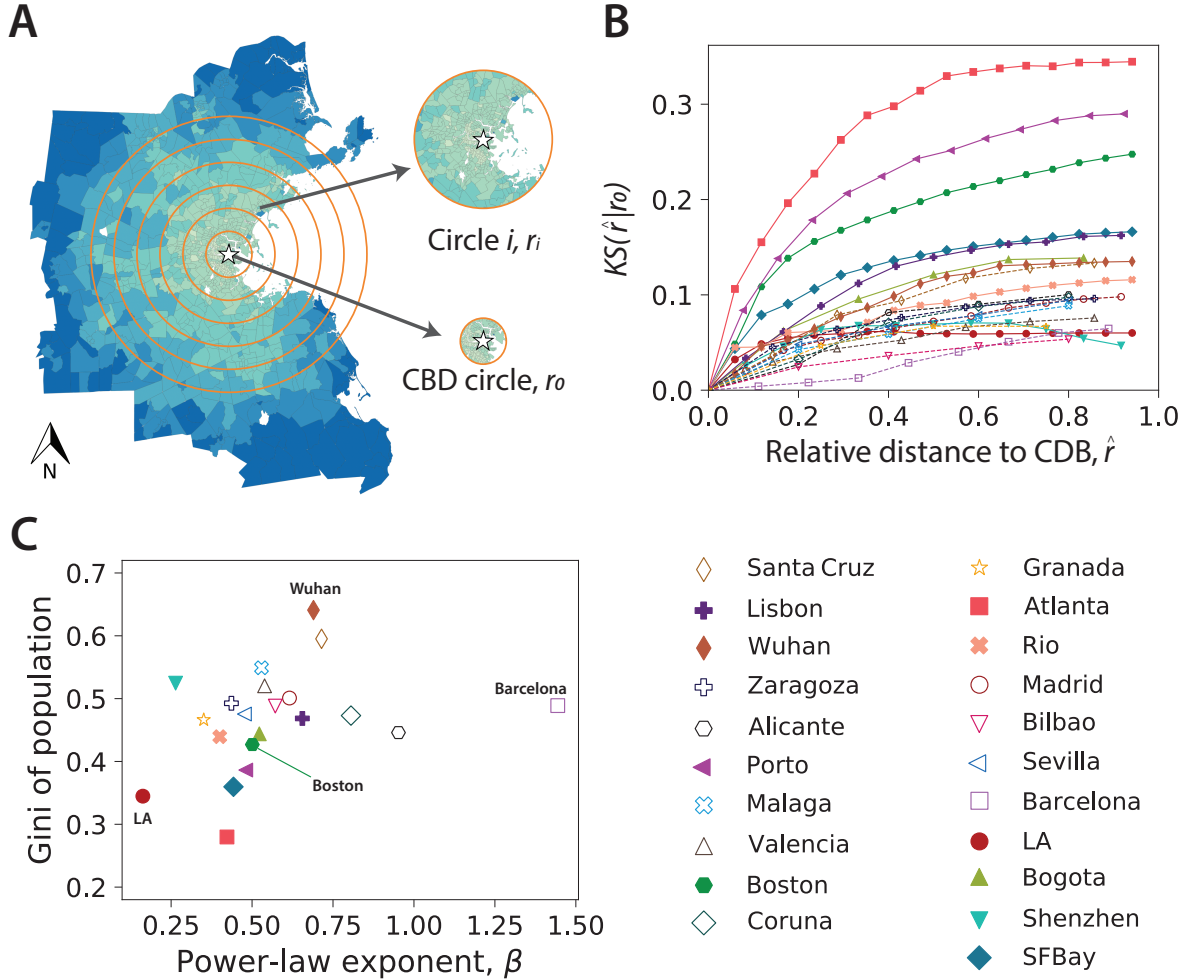


**Supplementary Fig. 8. Change of  $R_g$  in concentric rings at different distances to the CBD.**

(A) Box plot of the average  $R_g$  in the twenty-one cities in each ring. In the box plot, centre presents the median value of  $R_g$  for each census tract with a given distance to CBD; the bounds of box present the 25th and 75th percentile; whiskers present the interquartile range (IQR). (B) Box plot of the median  $R_g$  in the twenty-one cities in each ring. Only the first 7 rings are shown for the twenty-one cities. Both the average and median values show that, in general, the  $R_g$  values are relatively larger for the population residing further away from the CBD in the twenty-one cities, especially from the perspective of median  $R_g$ . There are 21 data points in each box in (A) and (B). Each point means one city.

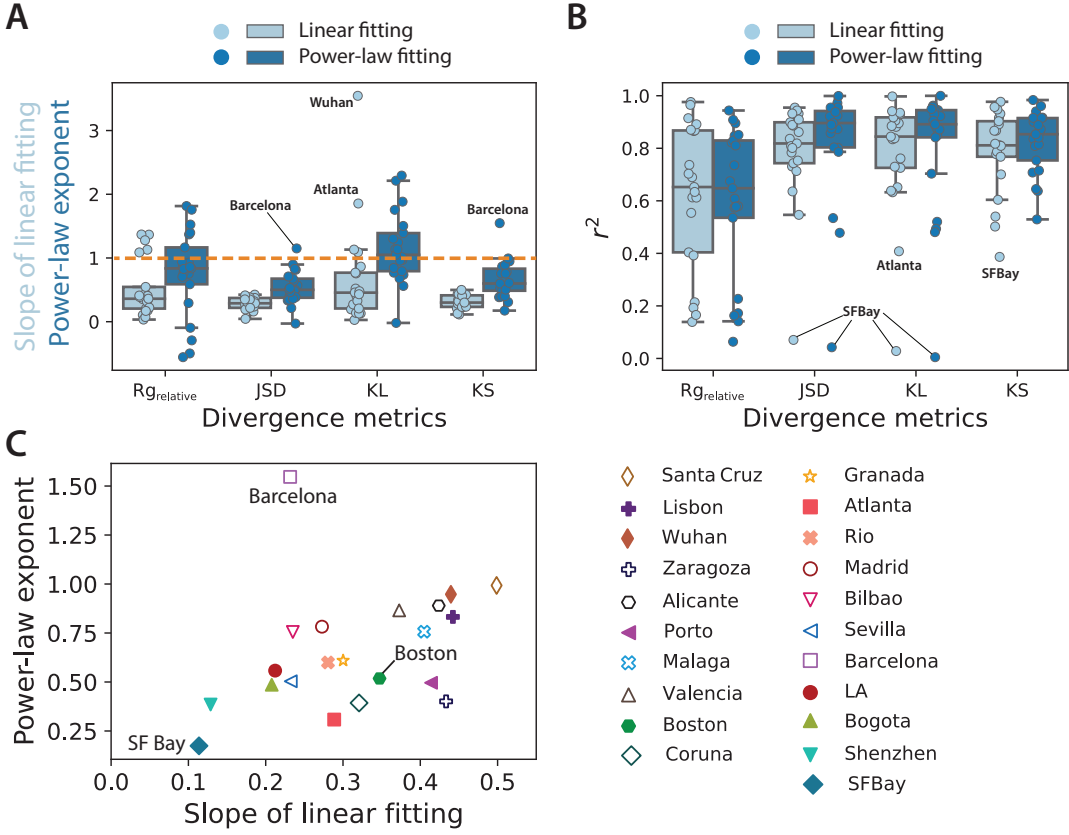


**Supplementary Fig. 9. Distribution of  $Rg$  in concentric rings at different distances to the CBD.** Cities are shown in descending order of  $\Delta KS_{typ}$ . Only the first 7 rings are shown for cities with radii over 21 km.



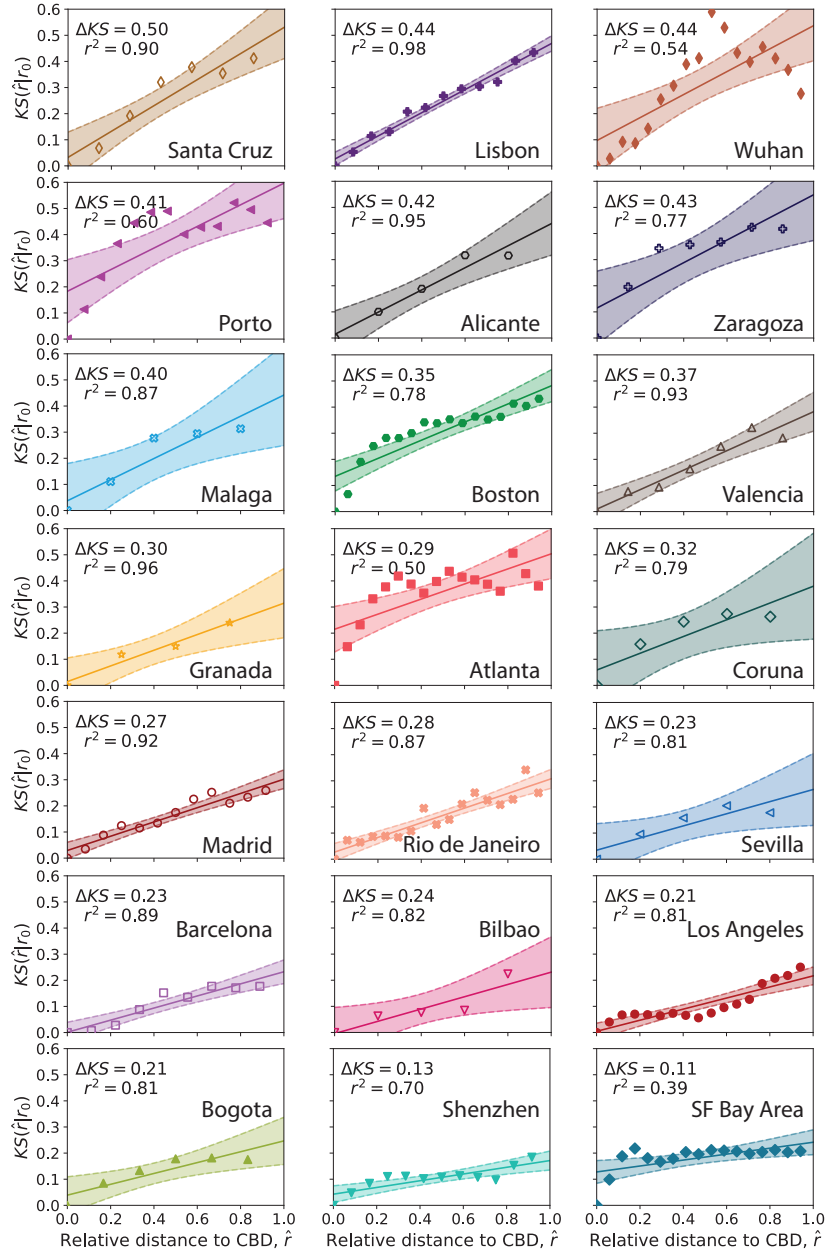
**Supplementary Fig. 10. Measuring urban structure via the statistical divergence of  $R_g$  values among concentric circles.** (A) Illustration of the CBD and outer circles centering at the CBD for a given city. In contrast to the definition in Fig. 2C, here the outer circle covers the CBD circle, leading to large overlapping between their  $R_g$  values, especially for very compact cities. (B) Relation between  $KS(\hat{r}|r_0)$  and the relative radii of the circles. As expected,  $KS(\hat{r}|r_0)$  is much more smooth than the way we calculate the change of  $R_g$  distributions in Fig. 2C. Thereby, we next utilize the power-law function to fit this relation. That is,  $\log(Y) \sim \beta \log(X) + \alpha$ ,  $\beta$  is the exponent of the power-law fitting. Here we use  $\beta$  to indicate

the urban structure. **(C)** Defining urban structure with Gini of population and the exponent of power-law fitting in **(B)**. We expect cities with larger  $\beta$  should be more monocentric because people's  $Rg$  values change faster with regard to the CBD. However, from this perspective, Boston falls between LA and Barcelona, two typical polycentric cities.

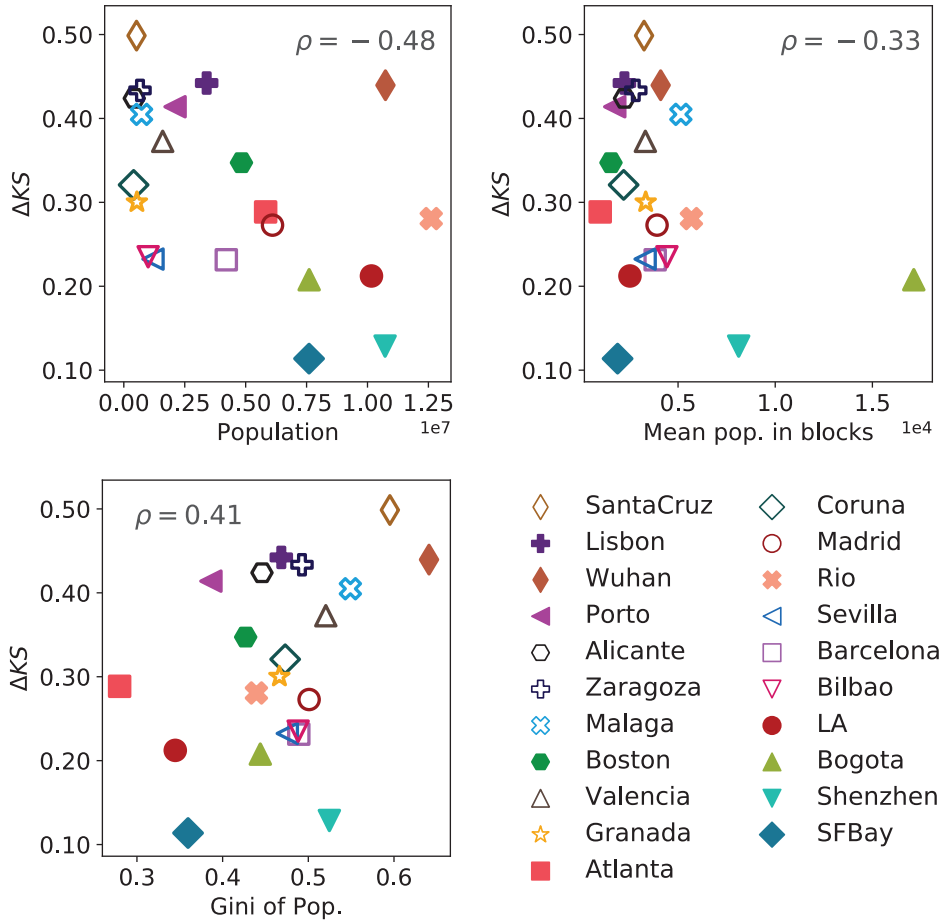


**Supplementary Fig. 11. Comparison of different statistical distance metrics to measure the divergence between the  $Rg$  values of the population.** We compare the KS distance with three other statistical distances. These are: (i)  $Rg_{relative}$ , relative change of the average  $Rg$ ; (ii) Jensen–Shannon divergence ( $JSD$ ); (iii) Kullback–Leibler divergence ( $KL$ ). Besides, for each statistical distance, we test both linear and power-law functions to fit the relation between the change of  $Rg$  and the distance to CBD, similar to the definition of  $\Delta KS$  in Fig. 2E. For the power-law function, we regard the fitted exponent as the urban structure metric. (A) Slope of linear fitting and power-law exponent for each statistical distance. There are cities with power-law exponents larger than 1.0 for all four metrics. For the linear fitting, only the metric with  $JSD$  and  $KS$  are limited to 0 and 1. In the box plot, the centre presents the median value of

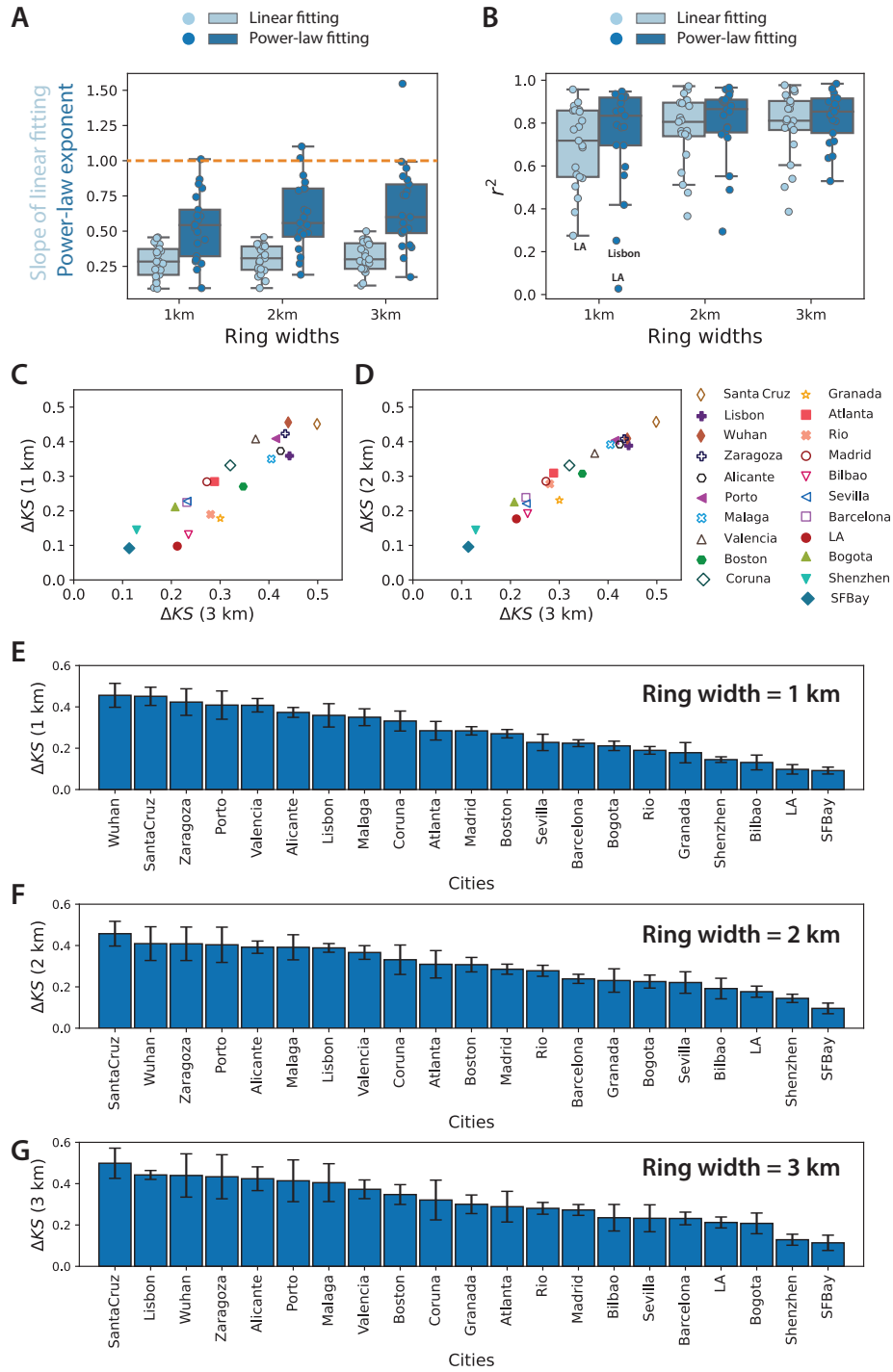
the Y-axis (slope of liner fitting or power-law exponent); the bounds of box present the 25th and 75th percentile; whiskers present the interquartile range (IQR). **(B)** R-square ( $r^2$ ) of linear and power-law fitting for each statistical distance. There are very low  $r^2$  values for the  $Rg_{relative}$ ,  $JSD$ , and  $KL$ . From this perspective, our proposed  $\Delta KS$  (slope of linear fitting on the  $KS$  distance) values are between 0 and 1 for all cities and perform well in terms of  $r^2$ . There are 21 data points in each box in **(A)** and **(B)**. Each point means one city. In the box plot, the centre presents the R-square value of the liner fitting or power-law fitting; the bounds of box present the 25th and 75th percentile; whiskers present the interquartile range (IQR). **(C)** Comparison between the power-law exponent and the slope of linear fitting for the  $KS$  statistic. Same as panel **A**, we can see that Barcelona is an outlier if we fit the change of  $KS$  with power-law function. Besides, if we regard the power-law exponent as an indicator of urban structure, the structure of Boston would fall between the structures of San Francisco Bay Area and Barcelona. Whereas, Boston is a typical monocentric city and both San Francisco Bay Area and Barcelona are polycentric.



**Supplementary Fig. 12. Linear fitting between  $KS(\hat{r}|r_0)$  and the relative distance to CBD  $\hat{r}$  for the twenty-one cities.** Cities are shown in descending order of  $\Delta KS$ . The color bands present the 95% confidence intervals of the linear fitting. The  $r^2$  is over 0.5 for most cities, except for SF Bay Area, which has an irregular spatial topology in comparison with the others.

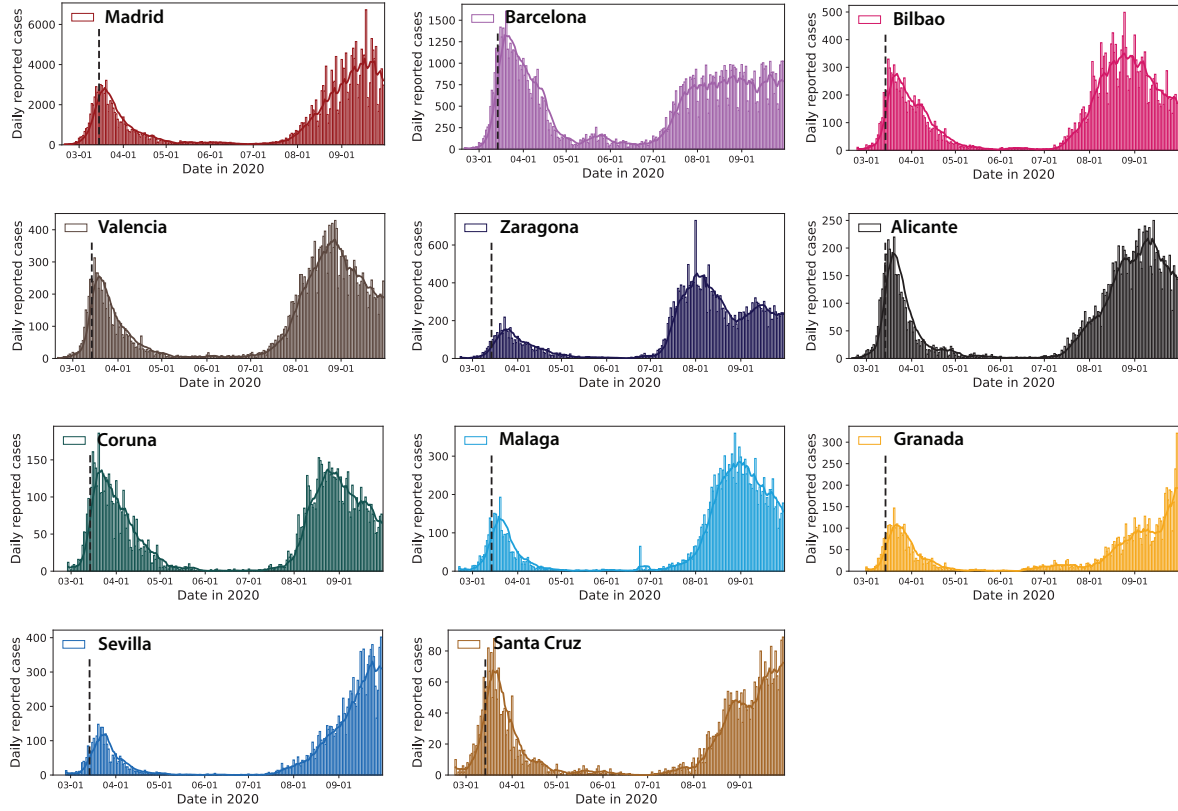


**Supplementary Fig. 13. Relation between  $\Delta KS_{typ}$  and the population distribution in the twenty-one cities.** Cities in the legend are ranked by their  $\Delta KS_{typ}$  in descending order.  $\Delta KS_{typ}$  is found having a negative relation to the total population in cities, except for Wuhan and Rio de Janeiro, but has a positive relation to the Gini of population.  $\Delta KS_{typ}$  has a relatively weak relation to the average population in blocks.



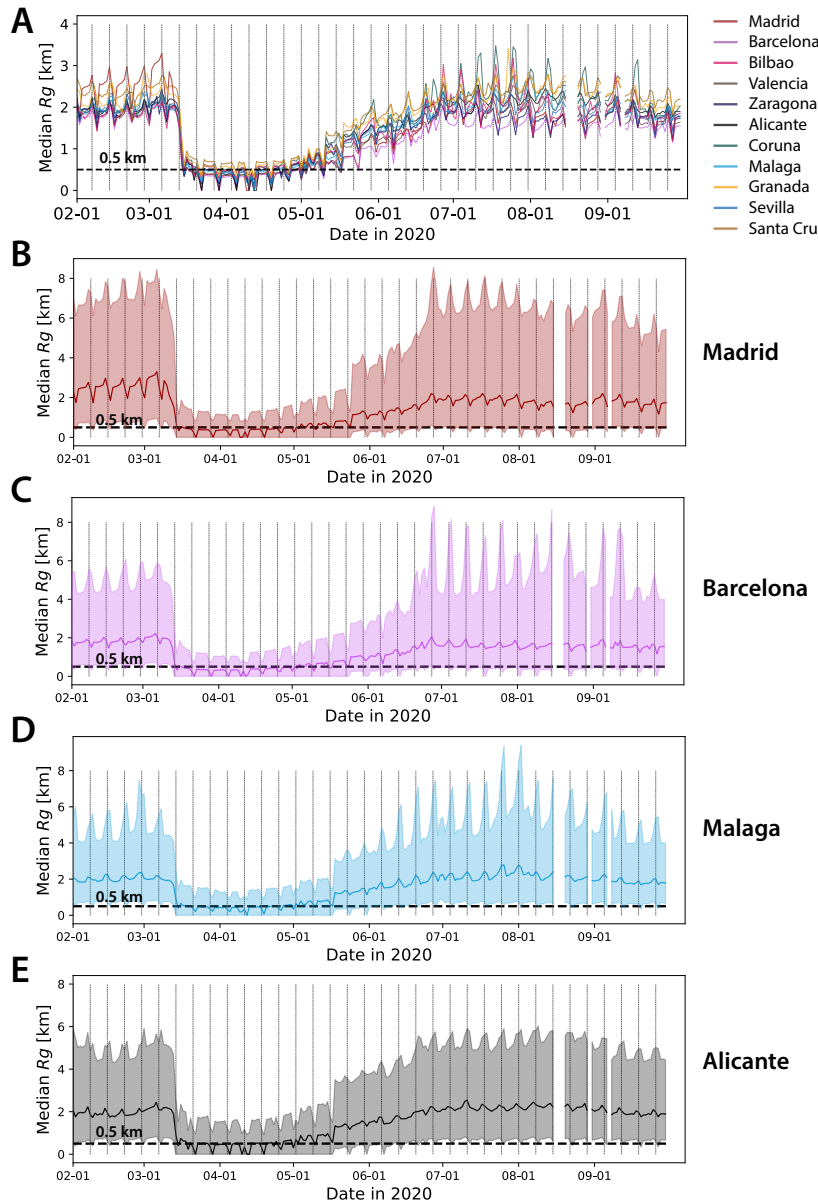
**Supplementary Fig. 14. Comparison of different ring widths in the definition of urban**

**structure.** **(A)** Slope of the linear and exponent of the power-law fit while grouping population in cities with varying ring widths. The slope of linear fitting has a similar range for the three widths. The exponent of the power-law function can be larger than 1. We prefer the mobility centrality index to be a value between 0 and 1. From this perspective, the slope of linear fitting is slightly better than the exponent of power-law fitting. In the box plot, the centre presents the median value of the Y-axis (slope of liner fitting or power-law exponent); the bounds of box present the 25th and 75th percentile; whiskers present the interquartile range (IQR). **(B)** R-square of linear and power-law fitting for varying ring widths. Results show that the 3 km width presents slightly better goodness-of-fit than 1 km and 2 km. There are 21 data points in each box in **(A)** and **(B)**. Each point means one city. In the box plot, the centre presents the R-square value of the liner fitting or power-law fitting; the bounds of box present the 25th and 75th percentile; whiskers present the interquartile range (IQR). **(C-D)** Comparison of  $\Delta KS$  between 3 km ring width and 1 and 2 km widths, respectively. **(E-G)** Ranks of cities from monocentric to polycentric structure for the definition with different ring widths. The bar height means the value of  $\Delta KS$  and the error bar means the standard (STD) error of the fitting of  $\Delta KS$ . We can notice cities are ranked in similar order. That means our  $\Delta KS$  metric does not depend on the width of the concentric rings.

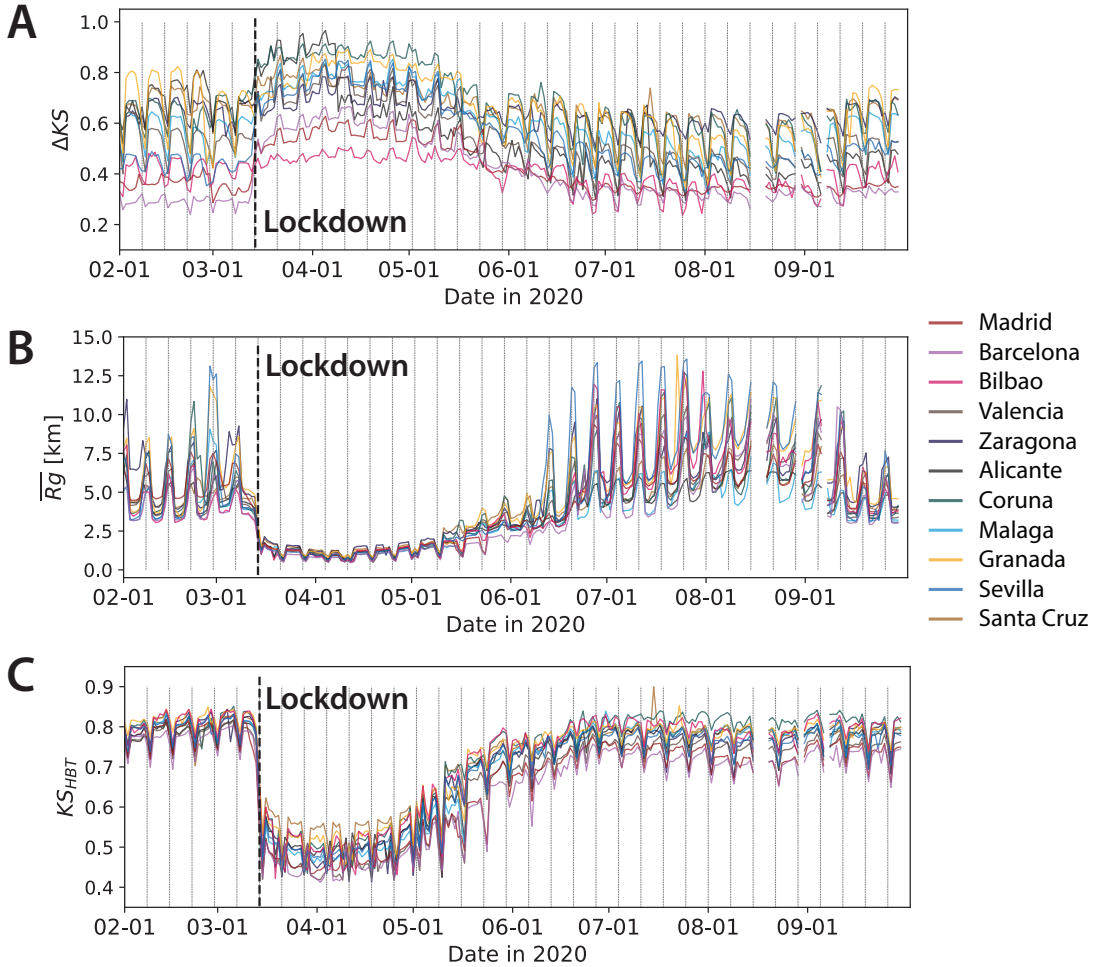


### Supplementary Fig. 15. Number of newly confirmed infections on each day by province.

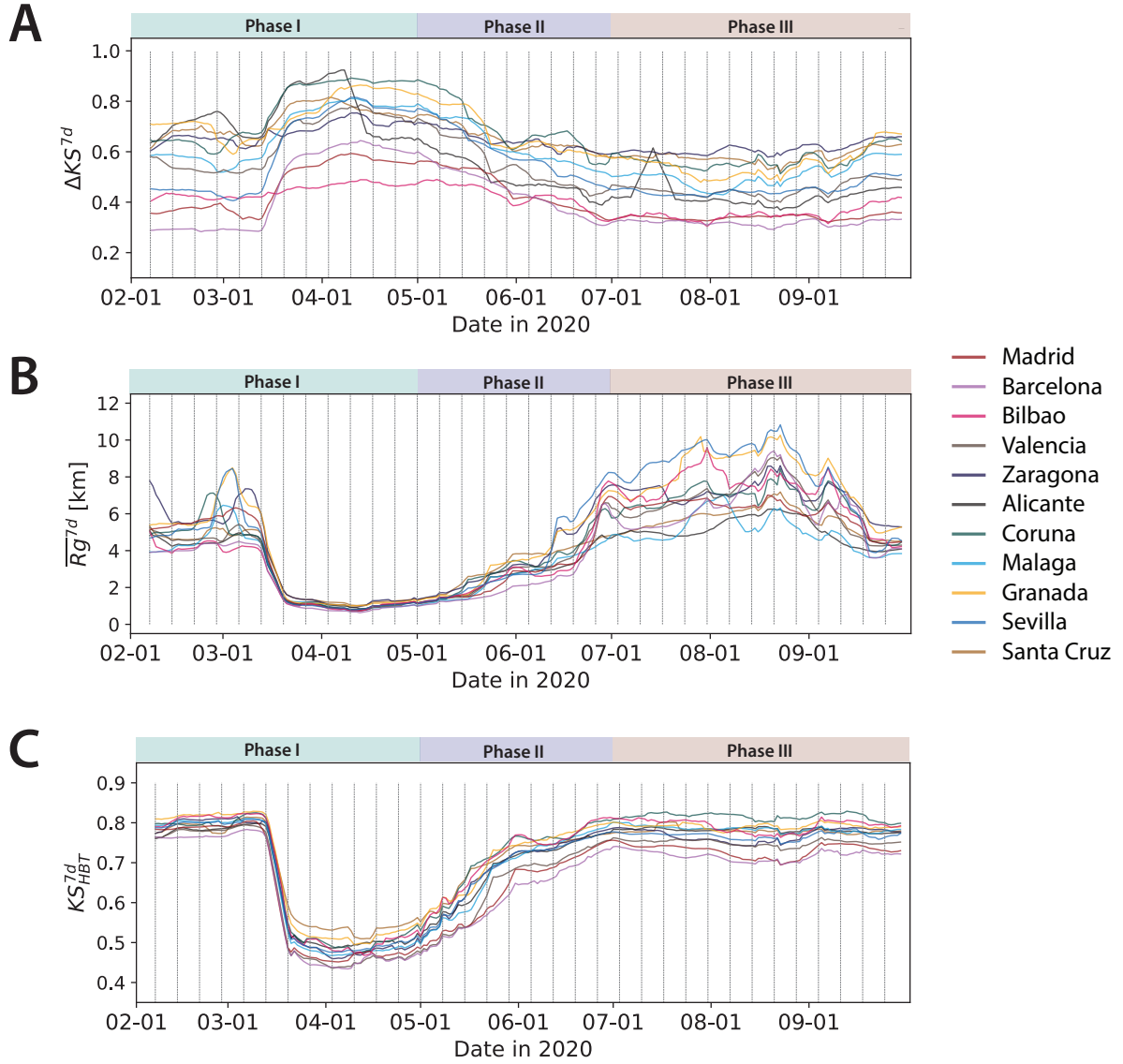
The bar plots depict the number of reported cases. The solid color lines depict the moving average number in the 7-day window from  $d - 6$  to  $d$ . A nationwide lockdown was imposed on March 14th, 2020, indicated by the dashed vertical lines. The national lockdown took effect in all cities in March, but the newly confirmed cases start to increase again in July 2020.



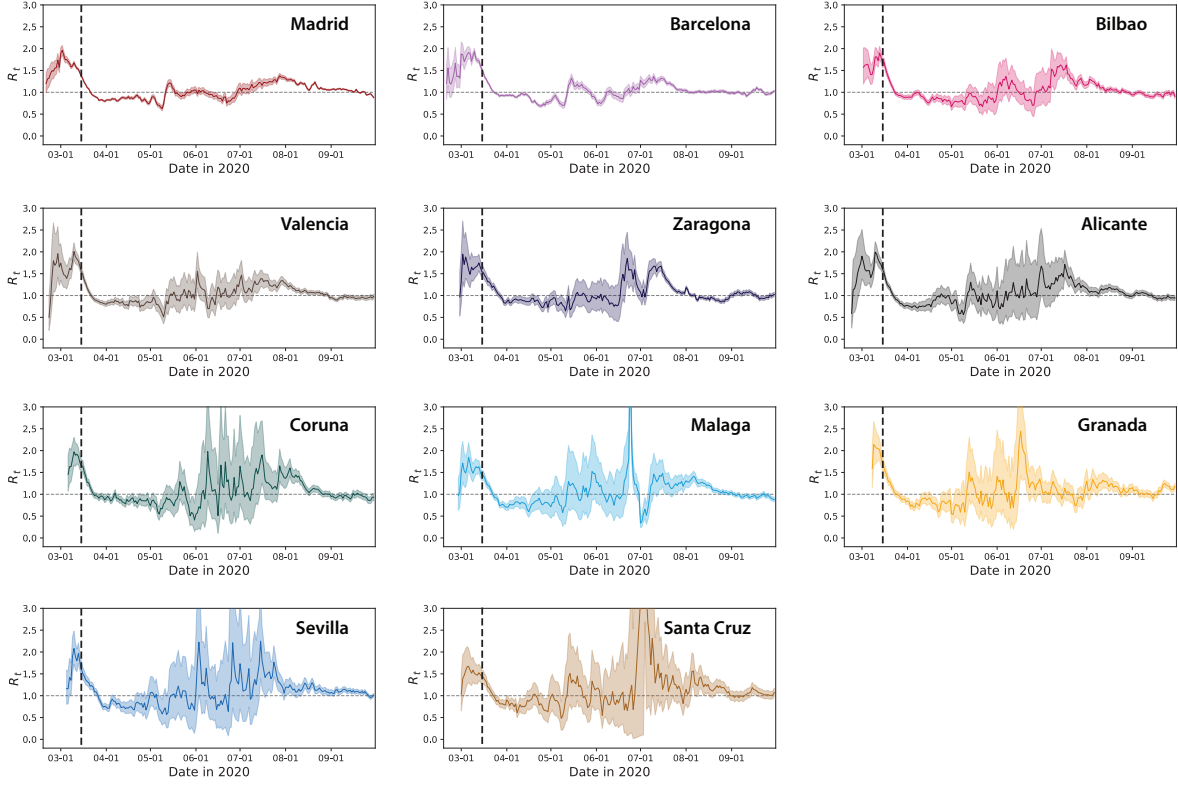
**Supplementary Fig. 16. Change of median  $R_g$  from February to September 2020 in the eleven Spanish cities.** (A) Median value of daily observed  $R_g$  in the eleven Spanish cities. During the national lockdown, the median  $R_g$  kept around 0.5 km for all cities. (B-E) Median  $R_g$  and the 25% – 75% confidence interval in two big cities (Madrid and Barcelona), and two relatively small cities (Malaga and Alicante).



**Supplementary Fig. 17. Daily observations of urban structure and mobility metrics in eleven Spanish cities** (A) Daily mobility centrality index  $\Delta KS^d$ . (B) Daily average  $Rg$ ,  $\overline{Rg}^d$ . (C) Daily observed  $KS_{HBT}$ ,  $KS_{HBT}^d$ . The dashed vertical lines indicate Saturdays from February 1st to September 30th, 2020. We have missing data from August 16th to 19th, on August 30th, and on September 7th. All three mobility metrics display weekly periodicity. The  $KS_{HBT}^d$  is between 0 and 1 and makes it easier to compare various cities. The mobility behavior started to recover in May. These observations help to monitor the weakening of the restriction policies and could be an early warning sign of the resurgence of the COVID-19 infections.



**Supplementary Fig. 18. 7-day averaged urban structure and mobility metrics.** The first vertical dashed line indicates February 7, corresponding to the average value during the first week in February 2020. The newly proposed  $KS_{HBT}$  displays much more stable behavior compared to the  $\overline{Rg}$  in all cities.



**Supplementary Fig. 19. Estimated time-varying reproduction number per city.** As the daily confirmed COVID-19 cases are not officially released in the 11 studied cities, we use the reproduction numbers in their provinces as proxies for the cities. To achieve a stable estimation, the  $R_t$  value on day  $d$  was fitted with the incidences during the 7-day time window from  $d - 6$  to  $d$  using the *EpiEstim* R package (10). The colored buffer shows 95% confidence interval of the estimation. The dashed vertical lines indicate the date of the national lockdown, March 14th, 2020.

**Supplementary Table 1. Goodness-of-fit of the linear fit to calculate the mobility centrality index  $\Delta KS$ .** We perform t-test for the linear regression and report the p-value in the table.

City	Country	$\Delta KS$	$r^2$	p-value	Standard error*
Santa Cruz	Spain	0.4987	0.9031	0.001	0.0731
Lisbon	Portugal	0.4422	0.9770	0.0	0.0215
Wuhan	China	0.4396	0.5402	0.0008	0.1047
Zaragoza	Spain	0.4334	0.7678	0.0097	0.1066
Alicante	Spain	0.4239	0.9477	0.0052	0.0575
Porto	Portugal	0.4139	0.6039	0.0018	0.1011
Malaga	Spain	0.4049	0.8669	0.0215	0.0916
Valencia	Spain	0.3727	0.9312	0.0004	0.0453
Boston	USA	0.3474	0.7778	0.0	0.0479
La Coruna	Spain	0.3208	0.7875	0.0446	0.0962
Granada	Spain	0.3002	0.9571	0.0217	0.0450
Atlanta	USA	0.2886	0.5021	0.0015	0.0742
Rio de Janeiro	Brazil	0.2806	0.8672	0.0	0.0284
Madrid	Spain	0.2728	0.9156	0.0	0.0262
Bilbao	Spain	0.2351	0.8174	0.0351	0.0642
Sevilla	Spain	0.2324	0.8091	0.0377	0.0652
Barcelona	Spain	0.2316	0.8911	0.0001	0.0306
Los Angeles	USA	0.2122	0.8105	0.0	0.0265
Bogotá	Colombia	0.2078	0.8112	0.0143	0.0501
Shenzhen	China	0.1287	0.7005	0.0007	0.0266
San Francisco Bay Area	USA	0.1137	0.3866	0.0077	0.037

\* Standard error of the estimated slope (gradient) of linear regression, under the assumption of residual normality.

**Supplementary Table 2. Fraction of population between city and province for the selected Spanish cities.**

City	Population (million)	Provincial Population (million)	Fraction
Madrid	6.102	6.663	91.6%
Barcelona	4.205	5.665	74.2%
Valencia	1.595	2.565	62.2%
Alicante	0.429	1.859	23.1%
La Coruna	0.402	1.120	35.9%
Zaragoza	0.663	0.965	68.7%
Sevilla	1.197	1.942	61.6%
Malaga	0.728	1.662	43.8%
Bilbao	0.999	1.153	86.6%
Santa Cruz	0.521	1.033	50.4%
Granada	0.536	0.915	58.6%

## References

1. A. Cori et al., EpiEstim R package, <https://cran.r-project.org/web/packages/EpiEstim/index.html> (2020). [Online; accessed 01-May-2020].
2. S. Jiang, *et al.*, The TimeGeo modeling framework for urban mobility without travel surveys, *Proceedings of the National Academy of Sciences* **113**, E5370–E5378 (2016).
3. Y. Xu, S. Çolak, E. C. Kara, S. J. Moura, M. C. González, Planning for electric vehicle needs by coupling charging profiles with urban mobility, *Nature Energy* **3**, 484–493 (2018).
4. M. De Nadai, Y. Xu, E. Letouzé, M. C. González, B. Lepri, Socio-economic, built environment, and mobility conditions associated with crime: A study of multiple cities, *Scientific Reports* **10**, 13871 (2020).
5. H. Theil, A. J. Finizza, A note on the measurement of racial integration of schools by means of informational concepts, *Journal of Mathematical Sociology* **1**, 187–194 (1971).
6. S. F. Reardon, D. O’Sullivan, Measures of spatial segregation, *Sociological Methodology* **34**, 121–162 (2004).
7. M. Ellis, R. Wright, V. Parks, Work together, live apart? Geographies of racial and ethnic segregation at home and at work, *Annals of the Association of American Geographers* **94**, 620–637 (2004).
8. G. Le Roux, J. Vallée, H. Commenges, Social segregation around the clock in the Paris region (France), *Journal of Transport Geography* **59**, 134–145 (2017).
9. Y. M. Park, M.-P. Kwan, Beyond residential segregation: A spatiotemporal approach to examining multi-contextual segregation, *Computers, Environment and Urban Systems* **71** (2018).

10. A. Cori, N. M. Ferguson, C. Fraser, S. Cauchemez, A new framework and software to estimate time-varying reproduction numbers during epidemics, *American Journal of Epidemiology* **178**, 1505–1512 (2013).
11. W. E. R. Team, Ebola virus disease in West Africa—the first 9 months of the epidemic and forward projections, *New England Journal of Medicine* **371**, 1481–1495 (2014).
12. N. R. Faria, *et al.*, Establishment and cryptic transmission of Zika virus in Brazil and the Americas, *Nature* **546**, 406–410 (2017).
13. S. Abbott, *et al.*, Estimating the time-varying reproduction number of SARS-CoV-2 using national and subnational case counts, *Wellcome Open Research* **5**, 112 (2020).
14. P. Nouvellet, *et al.*, Reduction in mobility and COVID-19 transmission, *Nature Communications* **12**, 1–9 (2021).
15. R. Lal, W. Huang, Z. Li, S. Prasad, An assessment of transmission dynamics via time-varying reproduction number of the second wave of the COVID-19 epidemic in Fiji, *Royal Society Open Science* **9**, 220004 (2022).
16. S. Ryu, D. Kim, J.-S. Lim, S. T. Ali, B. J. Cowling, Serial interval and transmission dynamics during SARS-CoV-2 delta variant predominance, South Korea, *Emerging Infectious Diseases* **28**, 407 (2022).